The Cryosphere Discuss., 7, 103–144, 2013
www.the-cryosphere-discuss.net/7/103/2013/
doi:10.5194/tcd-7-103-2013

The Cryosphere Discussions

High-resolution interactive modelling of the mountain glacier–atmosphere interface: an application over the Karakoram

E. Collier[1,2], T. Mölg[2], F. Maussion[2], D. Scherer[2], C. Mayer[3], and A. B. G. Bush[1]

[1]Department of Earth & Atmospheric Sciences, University of Alberta, Edmonton, Canada
[2]Chair of Climatology, Technische Universität Berlin, Berlin, Germany
[3]Commission for Geodesy and Glaciology, Bavarian Academy of Sciences and Humanities, Munich, Germany

Received: 12 November 2012 – Accepted: 7 December 2012 – Published: 4 January 2013

Correspondence to: E. Collier (eec@ualberta.ca)

Published by Copernicus Publications on behalf of the European Geosciences Union.

Abstract

The traditional approach to simulations of alpine glacier mass balance (MB) has been one-way, or offline, thus precluding feedbacks from changing glacier surface conditions on the atmospheric forcing. In addition, alpine glaciers have been only simply, if at all, represented in atmospheric models to date. Here, we extend a recently presented, novel technique for simulating glacier–atmosphere interactions without the need for statistical downscaling, through the use of a coupled high-resolution mesoscale atmospheric and physically-based mass balance modelling system that includes glacier MB and energy balance feedbacks to the atmosphere. We compare the model results over the Karakoram region of the northwestern Himalaya with both remote sensing data and in situ glaciological and meteorological measurements for the ablation season of 2004. We find that interactive coupling has a localized but appreciable impact on the near-surface meteorological forcing data and that incorporation of MB processes improves the simulation of variables such as land surface temperature and snow albedo. Furthermore, including feedbacks from the MB model has a non-negligible effect on simulated mass balance, reducing modelled ablation, on average, by 0.1 m w.e. (−6.0 %) to a total of −1.5 m w.e. between 25 June–31 August 2004. The interactively coupled model shows promise as a new, multi-scale tool for explicitly resolving atmospheric-MB processes of mountain glaciers at the basin scale.

1 Introduction

Spatially-distributed simulations of glacier mass balance require distributed meteorological forcing; however, obtaining this data is complicated both by the spatial and temporal scarcity of in situ observations and by the "scale mismatch" between the spatial scales represented in atmospheric models and those relevant for MB calculations (e.g. Machguth et al., 2009; Mölg and Kaser, 2011). To overcome these issues, forcing data can be obtained by extrapolation from point measurements by automated weather

TCD
7, 103–144, 2013

stations, where available, or interpolation from climate reanalyses and atmospheric model output, using surface- and free-air lapse rates. Surface lapse rates exhibit significant spatial and temporal variability, however, leading to uncertainty in temperature downscaling from altitude changes (Marshall et al., 2007; Gardner et al., 2009; Petersen and Pellicciotti, 2011). In addition, the assumption of linear lapse rates over glacier surfaces may not be appropriate (Petersen and Pellicciotti, 2011) and may under-predict surface temperature over debris-covered regions (Reid et al., 2012). Finally, additional corrections are often required for the poor representation of the strength and spatial variability of processes relevant to mass balance, such as orographic precipitation, in coarse spatial-resolution atmospheric models (e.g. Paul and Kotlarski, 2010; Radić and Hock, 2011).

Dynamical downscaling has been used to address the issue of spatial resolution in the most recent studies to produce climate data at horizontal resolutions of ∼ 18-km (Machguth et al., 2009; Kotlarski et al., 2010a,b; Paul and Kotlarski, 2010), ∼ 11-km (Van Pelt et al., 2012) and ∼ 1–3-km grid spacings (Mölg and Kaser, 2011; Mölg et al., 2012a,b) as forcing for distributed alpine glacier mass-balance calculations. This approach provides high spatial- and high temporal-resolution atmospheric fields obtained from a physical model, and the increased resolution allows for improved representation of features such as complex topography and orographic precipitation (e.g. Maussion et al., 2011). However, most of these studies required statistical corrections to link mesoscale circulation patterns and meteorological fields simulated by regional atmospheric models to local conditions on the glacier surface. Mölg and Kaser (2011) first showed that, at sufficiently high spatial resolution (∼ 1 km), a regional atmospheric model could be used to force explicit distributed simulations of glacier mass balance without statistical corrections at the glacier–atmosphere interface. This approach has since been applied successfully in multiple locations for small glaciers (Mölg and Kaser, 2011; Mölg et al., 2012a,b).

The traditional approach to simulations of mass balance, including those discussed above, has been one-way, or offline, in which meteorological fields are passed to the

TCD
7, 103–144, 2013

MB model but changing surface boundary conditions due to MB processes are not fed back into the atmospheric model. Interactively- or two-way-coupled atmospheric and ice-sheet simulations with simple treatments of ablation have been performed to estimate the paleoclimate and future climate behaviour of the Laurentide ice sheet, with significant alterations to atmospheric circulation, temperature and precipitation resulting from ice sheet evolution (Ridley et al., 2005; Pritchard et al., 2008). Although an initial effort has been made to include "interactive" alpine glaciers in a regional atmospheric model with the subgrid-scale parameterization of Kotlarski et al. (2010b), the influence of two-way coupling on the atmospheric forcing and explicitly simulated mass balance has yet to be assessed for alpine glaciers.

Here, we build on a new, unified and explicit approach to resolving the glacier–atmosphere interface without statistical downscaling (Mölg and Kaser, 2011), through the use of an interactively-coupled high-resolution mesoscale atmospheric and physically-based MB modelling system. By allowing changes in glacier surface conditions to feed back on the atmospheric drivers, the model provides a consistent calculation of surface energy and mass fluxes. For the initial application of the coupled model, we simulate the Karakoram region of the northwestern Himalaya (Fig. 1), which is estimated to contain anywhere from $\sim$ 1250–4000 km^3 of ice, covering an area of $\sim$ 18 000 km^2 (Bolch et al., 2012). Due to its extensive glaciation, this region presents a high potential influence on atmospheric simulations resulting from the inclusion of feedbacks from alpine glaciers. In addition, Yao (2007) estimates that more than half of the glaciated area is contained in the 15 largest glaciers, thus optimizing the Karakoram for representation in a high-resolution atmospheric model, where the smallest practical grid spacing is on the order of a few kilometers.

The Karakoram is also of interest due to recent evidence of stable or positive mass balances (e.g. Hewitt, 2005; Scherler et al., 2011; Gardelle et al., 2012; Kääb et al., 2012), which contrasts with the general trend of mass loss exhibited by glaciers elsewhere in the Himalaya (Cogley, 2011). However, definitive statements about the mass balance of Karakoram glaciers have been hampered by a dearth of both in situ

TCD
7, 103–144, 2013

measurements and information on ice thickness changes. The latter limitation has been partially addressed by recent geodetic studies (Gardelle et al., 2012; Kääb et al., 2012) that support reduced mass loss or even a positive mass balance anomaly in the early 21st century but emphasize the spatial and temporal heterogeneity of recent glacier behaviour. In addition, explicit, physically-based, spatially-distributed numerical modelling has the potential to clarify the dynamics occurring in this region.

In this study, we aim to (1) evaluate the performance of the coupled model against available measurements, (2) explore the importance of energy and mass exchanges between the glacier surface and boundary layer on the atmospheric forcing, and (3) assess the ultimate influence of interactive coupling on simulations of glacier mass balance. A final goal of this work is to improve the representation of alpine glaciers in mesoscale atmospheric models by introducing additional, relevant physical processes.

2 Methodology

The coupled modelling system (hereafter "WRF-MB") consists of two components: the advanced research version of the nonhydrostatic and fully-compressible Weather Research and Forecasting (WRF) mesoscale atmospheric model version 3.4 (Skamarock and Klemp, 2008, Sect. 2.1) and the process-based surface energy and MB model of Mölg et al. (2008, 2009, 2012a, Sect. 2.2). The MB model has been incorporated into the WRF source code as an additional physics option, and, thus, the user may select via runtime ("namelist") options whether the MB simulation is offline (conventional one-way forcing, with feedbacks only from WRF's land surface model) or interactive (feedback from MB model to WRF over glaciated grid cells; Sect. 2.3). We performed two simulations, one interactive (INT) and one offline (OFF), for the months of June–August 2004, to coincide with a limited number of glaciological and meteorological measurements available for evaluation (Sect. 2.4), with the period of 1–25 June discarded as model spin-up time. As a first approximation, we focused on the meteorologically-driven fluctuations of mass balance and neglected the influence of debris cover.

TCD
7, 103–144, 2013

2.1 Mesoscale atmospheric model

For these simulations, WRF was configured with three nested domains of 33-, 11- and 2.2-km spatial resolution, centered over the northwestern Himalaya (D1–3; Fig. 1). By increasing the spatial resolution over the region of interest, the use of multiple grid nesting improves the representation of complex terrain and associated processes such as orographic precipitation, and has been found to increase the simulation skill of WRF for mountain summit conditions (Mölg and Kaser, 2011). Model physics and other settings were selected following the recommendations of the National Center for Atmospheric Research (NCAR) for regional climate simulations with WRF (Table 1; outlined in WRF ARW user's guide). Note that no cumulus parameterization was employed in the highest-resolution model domain, WRF D3 (e.g. Molinari and Dudek, 1992; Weisman et al., 1997). The range of terrain elevation represented in this domain at 2.2-km resolution is 916 to 7442 m a.s.l., which encompasses the most heavily glaciated altitudes in the Karakoram (~ 2700–7200 m, as shown in Fig. S2 of Bolch et al. (2012), with the mean basin-wide glacier elevation located at 5326 m).

In this study, WRF was coupled with the Noah land surface model (LSM; Chen and Dudhia, 2001). The land-ice mask was updated using glacier outlines for the Karakoram region based on the glacier inventory of China (Shi et al., 2012) as well as inventories generated by ICIMOD (2007) and GlobGlacier (Frey et al., 2012). Other modifications made to glaciated grid cells included assigning (1) zero vegetation cover, (2) maximum and minimum albedo values consistent with the parameterization in the MB model (Sect. 2.2), and (3) a soil moisture availability of 1.0 (from an original value of 0.95). The conventional bulk computation of the latent heat flux in the WRF surface module is multiplied by the last parameter; therefore, this change was made for consistency with the MB model.

The atmospheric model was forced with ERA-Interim data at $0.75 \times 0.75^{\circ}$ spatial-resolution and 6-hourly temporal-resolution, as provided by the European Centre for Medium-Range Weather Forecasts (ECMWF; Dee et al., 2011). In the ERA-Interim

TCD
7, 103–144, 2013

reanalysis, snow depth is arbitrarily set to 10 m in the analysis for grid cells with greater than 50 % glacier coverage (Dr. Paul Berrisford, personal communication, 2012), which results in unphysical snow depths over the Karakoram. We therefore obtained the initial snow condition from the microwave-derived Global EASE-Grid 8-day Blended SSM/I and MODIS Snow Cover SWE data (Brodzik et al., 2007), assuming a snow density of 300 $kg\,m^{-2}$ and assigning an initial depth of 2 m over large glaciers where the data are missing (less than 0.1 % (8 in total) of data points in the region spanned by WRF D1).

WRF employs a terrain-following hydrostatic-pressure coordinate in the vertical, defined as eta (η) levels (Skamarock and Klemp, 2008). For these simulations, the lowest atmospheric model level was specified at $\eta = 0.997585$ (~ 20 m) to maintain the validity of the constant-flux assumption in the bulk computation of the turbulent heat fluxes, as the surface mid-layer height (less than 10 m) is used in the calculation following the approach of the Noah LSM. We selected the recently revised Monin–Obukhov surface layer (Jiménez et al., 2012), which was found to improve the simulation of the diurnal amplitudes of near-surface meteorological fields over complex terrain with a horizontal spatial resolution of 2 km. We also used positive-definite explicit 6th order diffusion (Knievel et al., 2007), in order to dampen small-scale noise in the atmospheric fields and because Mölg and Kaser (2011) found this option improved the simulated magnitude of precipitation at high elevations on Kilimanjaro. For the simulations presented here, we selected the default value of the diffusion coefficient (0.12) for all model domains except D3, for which we used a value of 0.36. The choice of the diffusion parameter value is uncertain, and thus we also performed test runs varying the parameter in D3 from 0.12 to 0.6. Values below 0.36 resulted in a noticeable decrease in precipitation over the Karakoram that was not in agreement with the in situ measurements discussed in Sect. 2.4, while higher values had a only a small effect.

2.2 Surface energy and mass balance model

The MB model is described fully by Mölg et al. (2008, 2009) with the most recent updates in Mölg et al. (2012a), but we will review some important features here. The

TCD
7, 103–144, 2013

model computes the column specific mass balance from solid precipitation, surface deposition and sublimation, surface and subsurface melt, and refreeze of both meltwater and liquid precipitation. To determine the mass fluxes, the model first solves the surface energy balance equation,

$$S\downarrow \cdot (1 - \alpha) + L\downarrow + L\uparrow + \mathrm{QS} + \mathrm{QL} + \mathrm{QG} + \mathrm{QPRC} = F_{\mathrm{NET}} \quad (1)$$

in which the terms correspond to, from left to right: incoming shortwave radiation, broadband albedo, incoming and outgoing longwave radiation, turbulent fluxes of sensible and latent heat, ground heat flux and heat flux from precipitation. The ground heat flux, QG, consists of a conductive component (QC) as well as a component due to subsurface penetration of shortwave radiation (QPS). The net flux, F_{NET}, represents the energy available for melt, QM, provided the surface temperature is at the melting point, $T_{\mathrm{M}} = 273.15\,\mathrm{K}$.

The model treats both surface and subsurface processes, including surface albedo and roughness evolution based on snow depth and age; snowpack compaction and densification by refreeze; and the influence of penetrating solar radiation, refreeze and conduction on the englacial temperature distribution. Here, the MB model forcing every timestep consists of air temperature, humidity, winds, and air pressure, all of which were taken from the lowest model level ($z = 20\,\mathrm{m}$). Note that the diagnostically-updated 2- and 10-m meteorological fields were not used as forcing so as to (1) be consistent with the approach of the Noah LSM (Chen and Dudhia, 2001), and (2) prevent decoupling of the atmosphere and land surface, wherein the lower atmosphere is no longer influenced by surface conditions. The MB model also takes as input: total precipitation and its frozen fraction; incoming short- and long-wave radiation; and time between snowfall events. The initial subsurface temperature was specified through linear interpolation of the input data to the Noah LSM, available at 0.1, 0.4, 1.0, and 2.0 m depths, and assigning a constant value of 268.6 K below this level. The lower boundary is specified at 268.6 K during the simulation, based on measurements taken from a Tibetan

TCD
7, 103–144, 2013

glacier (Mölg et al., 2012a). We address uncertainties in the subsurface temperature initialization by including a long (25-day) model spin-up period.

2.3 Coupling architecture

For both offline and interactive simulations, the MB model calculates glacier surface energy and mass fluxes among other variables at every timestep (e.g. every 4 s in D3) over glaciated grid cells, while the Noah LSM values are retained over non-glaciated grid cells. The integrated modelling approach permits some advantages in the MB model forcing strategy. For example, topographic shading, incoming short- and long-wave radiation, and the fraction of frozen precipitation are now obtained from the atmospheric models surface, radiation, and microphysics modules, respectively. Another important advantage is that WRF provides high-resolution, dynamically-derived, and spatially-distributed forcing data without the need for traditional statistical methods, such as those mentioned in Sect. 1. The incorporation of the MB model adds negligible computational expense to WRF simulations.

For interactive simulations, the MB model updates over glaciated areas in WRF, at every timestep, (1) surface heat and moisture fluxes, (2) surface and subsurface (including deep soil) temperature, (3) snow depth, water equivalent and fractional cover, (4) surface albedo and roughness, and (5) surface specific humidity. The inclusion of feedbacks represents a more consistent approach, as it permits the near-surface forcing variables to be modified by exchanges of mass, momentum and moisture between the glacier and the atmospheric surface layer. In this study, the MB model output accumulated energy and mass fluxes every hour that were then converted into hourly averages for analysis; these data will be referred to as "hourly".

As indicated at the beginning of Sect. 2, it is not absolutely correct to label the two forcing approaches as "offline" and "interactive" because the atmospheric model currently receives surface feedbacks through the Noah LSM. There have been recent efforts to improve the simulation of snow processes in WRF, such as with the introduction of the Noah-MP land surface parameterization (Niu et al., 2011), which, for

TCD
7, 103–144, 2013

example, introduces separate vegetation canopy and surface layers and the possibility of multiple vertical layers in the snowpack. However, the simplified treatment of glacier grid cells in the Noah LSM is retained. Thus, by incorporating the MB model, we are able to simulate more physical processes relevant for glaciers, such as refreezing of meltwater in the snowpack, englacial melt, and formation of superimposed ice. Other improvements to the treatment of snow and ice physics, compared with the Noah LSM, include introducing multiple layers in the snowpack, increasing the column depth from 2 to 9 m, consideration of snow porosity, and allowing for full snowpack ablation to expose bare ice. The latter point is especially critical, as the Noah LSM imposes minimum snow depth and water equivalent values over land-ice grid cells.

2.4 Measurements for model evaluation

In Sect. 3.2, we compare the coupled model results with a limited number of available ablation stake measurements as well as automated weather station (AWS) data that were acquired in summer 2004 on the Baltoro glacier (35° 35′–35° 56′ N, 76° 04′–76° 46′ E; Mihalcea et al., 2006). The glacier is approximately 62 km long, with an average (maximum) width of 2.1 (3.1) km (Mayer et al., 2006). We use data from 6 sections (SF, U, G1, C, BN, and BS) as well as from a longitudinal transect along the glacier (L1, L2 and L3), comprising 53 stakes in total that provide sufficient spatial coverage (cf. Fig. 1b or 4b) to evaluate both the spatial pattern and the magnitude of ablation in the coupled model applied to the Baltoro glacier. The ablation measurements were taken at different intervals between 1–15 July 2004; a brief summary of the location and other details of the stake measurements are given in Table 3 (a more detailed description of the data can be found in Mihalcea et al. (2006)). While the data represent a brief period, they provide the only available direct ablation measurements in the Karakoram. For the comparison, total simulated surface lowering was interpolated to the mean location of the stake section or transect using inverse distance weighting.

The AWS was situated adjacent to the glacier on a moraine ridge at an elevation of 4022 m (35° 43.684′ N, 76° 17.164′ E) and provided hourly-mean data after 18 June

TCD
7, 103–144, 2013

2004 (Mihalcea et al., 2006). We compared this data with WRF data from the nearest model grid point (located at an elevation of 4322 m), which was also non-glaciated and therefore was more consistent in the land surface type. However, the data therefore do not include direct feedbacks from the MB model. Note that the assumptions discussed in Sect. 2.1 for snow initialization were not applied over the stake sites on the main glacier area (cf. Fig. 1b).

To supplement these field measurements, we also evaluate in Sect. 3.1 the basin-scale performance of the coupled model using MODIS/Aqua (1) MYD10A1 daily snow albedo available at 500-m resolution, and (2) MYD11A2 8-day land surface temperature available at 1-km resolution, with daily data obtained by averaging day- and night-time temperatures where both fields were available and were assigned the highest quality assurance flag for MODIS products. Due to the prevalence of missing data in the snow albedo dataset, we considered only the grid cells with at least 25 % valid observations during the 67-day period for comparison with WRF. Both MODIS datasets were re-projected to the WRF D3 grid before completing the analysis.

3 Results and discussion

We first compare our simulated results with remote sensing data (Sect. 3.1) and with meteorological and glaciological measurements from the Baltoro glacier (Sect. 3.2). The role of interactive coupling on the atmospheric forcing data and on simulations of mass balance will then be discussed. Results are presented from the finest-resolution atmospheric model domain only, since it provides the most realistic terrain representation.

3.1 Remote sensing data

Figure 2 presents a comparison between WRF-MB and the MODIS/Aqua datasets discussed in Sect. 2.4. The elevation profile of land surface temperature (LST) averaged

TCD
7, 103–144, 2013

over the simulation period produced by the MB model is in good agreement with the MODIS data above ∼ 5200 m and is an improvement on the Noah LSM values at all resolved elevations (Fig. 2a). The strong divergence of modelled and observed LST below 5200 m likely results from neglecting debris cover, since its presence allows the glacier surface to be warmed by solar radiation above the melting point. Supraglacial debris extent has also been found to increase with distance down glacier in remote-sensing case studies of the central Karakoram (e.g. Scherler et al., 2011). Specific to the Baltoro glacier and its tributaries, Mayer et al. (2006) found that debris coverage increased to 70–90 % of the glacier area below 5000 m, with 100 % coverage found below the U site (Fig. 1b). A time-series analysis of LST, averaged only over elevations greater than 5200 m is presented in Fig. 2b. The MB model gives an improved performance over the LSM alone, although LST is generally under-predicted, with mean biases of −1.0, −1.3, and −6.1 K in the INT, OFF, and Noah LSM simulations, respectively. Conversely, snow albedo in WRF-MB is in good agreement with MODIS below ∼ 5200 m (Fig. 2c), although simulated values are constrained by the lower bound of $\alpha_{ice} = 0.3$ as snow depth goes to zero and, thus, slightly overestimate the observational values at the lowest elevations. Above 5200 m, WRF-MB over-predicts snow albedo compared with MODIS. However, it produces values and an altitudinal gradient that are in much better agreement with observations than the Noah LSM.

The strong discrepancy between Noah LSM and MODIS data is in part related to the treatment of grid cells defined as glacial ice: the LSM imposes minimum values of snow depth and water equivalent of 0.5 and 0.1 m, respectively, thus preventing the exposure of bare ice or debris and the associated lowering of surface albedo. In addition, the Noah LSM employs a time-decaying snow albedo formulation (based on the scheme of Livneh et al., 2009) and determines surface albedo using fractional snow cover to correct a background snow-free albedo. Although snow albedo is likewise an exponential function of age in the MB model (following Oerlemans and Knap, 1998), the actual surface albedo also depends on snow depth to account for surface darkening

TCD
7, 103–144, 2013

when the snowpack is thin. It is clear from Fig. 2 that this formulation, in combination with permitting snow-free conditions, gives more realistic values.

The evaluation of modelled albedo is sensitive to the simulated timing of snowfall events for both models, due to the nature of the parameterization schemes, and is limited by the large number of missing data in MODIS. In addition, comparison is hindered by the fact that the MODIS daily albedo product is not a daily-averaged quantity (as the simulated data are) but rather a collection of pixels with the highest quality from that day for which acquisition time is not trivial to retrieve (Stroeve et al., 2006). Finally, the small positive biases in snow albedo below ~ 4300 m and the negative biases in LST are both physically consistent with neglecting the influence of debris cover in WRF-MB, as will be discussed further in Sect. 3.4.

3.2 Baltoro glacier

Figure 3 presents a time series of modelled and observed near-surface meteorological data from the Urdukas AWS that is situated adjacent to the Baltoro glacier. WRF-MB is skillful in simulating air temperature at 2 m, and its evolution over the study period, including capturing periods of reduced diurnal variability at the beginning and between 30 July and 6 August. The magnitude of the near-surface wind speed is also in agreement with the AWS data. However, an important discrepancy is the underestimation of precipitation at this particular grid cell in both INT and OFF simulations: the AWS records a total of 122.8 mm of precipitation between 25 June and 31 August, while INT and OFF simulate 46.9 and 48.4 mm, respectively. Missing precipitation events are also reflected as discrepancies in the time series of relative humidity (cf. Fig. 3b, e).

WRF-MB produces 40 to 80 cm of ablation along the main body of the Baltoro glacier between 1–15 July 2004 (Fig. 4a). Spatial comparison of the two simulations reveals only small differences, generally on the order of a few centimeters, consistent with the short nature of the study period (Fig. 4b). There are slightly positive anomalies at lower elevations, corresponding to less ablation in INT; conversely, there are negative anomalies at higher elevations, corresponding to more ablation in INT. Total simulated ablation

TCD
7, 103–144, 2013

is in order-of-magnitude agreement with measurements (Fig. 4c); however, the model overestimates ablation at all sites, in part because it does not capture four precipitation events, amounting to 17.6 mm, during the measurement period (cf. Fig. 3e). In comparing daily simulated/measured ablation rates and mean debris thickness (Table 4), the rates tend to be in better agreement for sites with thinner mean debris cover (SF, L2, L3, C) and more strongly overestimated by WRF-MB where supraglacial debris is thicker (U, L1, G1, BN, BS). Although differences between INT and OFF are small, INT is in closer agreement with observations at all but one site (BN, as a result of less simulated refreeze than in OFF), with the strongest improvement at BS. The improvement at this site stems from faster complete snowcover removal (~ 1 day earlier in INT), which reduces subsurface penetration of shortwave radiation and, thus, subsurface melt production. Finally, the overestimation of ablation by WRF-MB tends to diminish as the observation period increases (Fig. 4d), which then suggests that the coupled model as configured in this study may be best suited for "climatological" simulations of glacier mass balance due to its sensitivity to the timing of precipitation.

Mihalcea et al. (2008) performed distributed surface-energy sub-debris melt modelling, using the Urdukas AWS data as forcing for the same study period. The authors determined debris extent, thickness and thermal properties from satellite imagery, and considered only the elevation range of 3650–5400 m a.s.l., which gives a corresponding glacier area of 124 km^2. Mihalcea et al. (2008) computed 0.058 km^3 w.e. of ablation, or a mean surface lowering of 0.47 m between 1–15 July, which was found to be a slight underestimation (on average, −0.016 m) of the observed ablation rates at the SF site. For comparison, INT and OFF simulate 0.069 and 0.070 km^3 w.e. of surface melt, respectively, over an area of 126 km^2 that produces an average thickness change of approximately −0.55 m. The actual mass balance calculation in the MB model also includes additional processes, such as snowpack ablation and surface vapour fluxes, that bring the total simulated mass loss to 0.078 km^3 w.e. between 1–15 July. We employ the same glacier outline, that of Mayer et al. (2006); however, discrepancies in our estimates may arise from its projection to the WRF D3 grid, differences in removal

TCD
7, 103–144, 2013

of tributary glaciers, and the coarser representation of the Baltoro glacier at 2.2-km spatial resolution (vs. 90-m in Mihalcea et al., 2008). Despite these and other sources of disagreement, comparing the two estimates gives an approximate measure of the effect of neglecting debris, which is thought to cover 38 % of the Baltoro glacier (Mayer et al., 2006) and 73 % of the altitude range of the main glacier tongue considered in Mihalcea et al. (2008), in our simulations.

3.3 Influence of interactive coupling

Figure 5 presents a time series of daily means of the near-surface WRF meteorological data used as forcing for the MB model and provides the context for the fluctuations of surface energy and mass fluxes discussed in this section. Near-surface air temperatures in INT are warmer by 0.3 °C on average than in OFF (Fig. 5a). The difference arises primarily from a reduced amplitude of the diurnal cycle, with warmer nocturnal temperatures (Fig. 5a subpanel). INT simulates higher surface temperatures (T_{sfc}), as well as warmer subsurface temperatures in the top 0.5–1 m (peak differences are ~ 0.7 °C, not shown), as a result of stronger downward longwave radiative forcing (see Fig. 5f for daily average curves). The increase in $L\downarrow$ is expressed between evening and early morning (+4.2 W m^{-2} between 6:00 p.m. and 8:00 a.m. LT) and is a direct result of higher mixing ratios at 2 m in INT during this period (not shown). The change in radiative forcing in INT translates into less heat extraction from the surface layer, through a reduced nocturnal QS, and, in turn, into the near-surface temperature difference. Note that the near-surface air temperature evolution simulated in INT may represent an improvement, as Mölg et al. (2012b) previously found that WRF + Noah LSM can produce an excessively large diurnal cycle as a result of a nighttime cold bias at 2-m compared with AWS measurements on Kilimanjaro. Interactive coupling also results in an average reduction of incoming shortwave radiation (−9.0 W m^{-2}) and, as previously mentioned, a mean increase in incoming longwave radiation (2.4 W m^{-2}). The changes in downward radiation arise from alterations to atmospheric clouds and moisture: $\Delta_{INT-OFF}S\downarrow$ correlates inversely with mean vertical changes in cloud fraction

TCD
7, 103–144, 2013

($r = -0.44$), while $\Delta_{\mathrm{INT-OFF}} L\downarrow$ correlates more strongly with changes in mixing ratio ($r = 0.78$). Basin-scale daily-mean differences in the other forcing variables for the MB model (relative humidity, wind speed, precipitation and its frozen fraction, and surface pressure) are negligible (Fig. 5).

The atmospheric changes induced by including feedbacks from the MB model are generally small in magnitude and limited in vertical extent, but still appreciable. Air temperature and mixing ratio anomalies, on the order of 0.1 °C and 0.1 g kg^{-1}, are generally confined to the lowest 10 model levels, which correspond to the layer between a mean surface pressure of 543 hPa and the level of 450 hPa (Fig. 6a). Vertical changes in the mean cloud cover fraction are variable, with the greatest differences present near the levels of 375 ($\eta = 12$–14) and 125 hPa ($\eta = 26$–29; Fig. 6d). However, interactive coupling has a strong warming influence on the subsurface temperature distribution (Fig. 6c), as a result of (1) the inclusion of the energy flux from penetrating solar radiation, and (2) the method for updating deep soil temperature (T_{ds}), which is defined at a depth of 3 m. With regard to the latter point, T_{ds} in INT is taken from the MB model subsurface scheme, which resolves the column to a depth of 9 m but is constrained by a lower boundary temperature of 268.6 K in this study. In contrast, the Noah LSM updates T_{ds} using a weighted combination of the annual mean T_{sfc} of the previous year and of the last 150 days as the data become available, with no lower threshold imposed. As a result, the minimum values for T_{sfc} in the MB model and Noah LSM are $\sim$ 245 and 224 K, respectively, and subsurface temperatures are clearly warmer in the INT simulation.

The non-negligible influence of interactive coupling on the near-surface meteorological forcing data translates primarily into reduced ablation of snow and ice in INT (Fig. 7a, b). Area-averaged modelled surface height lowering is smaller and total mass balance is less negative in INT, with a mean reduction in ablation over the Karakoram basin of 0.1 m w.e. (−6.0 %), to a cumulative value of −1.5 m w.e. by 31 August. The difference in the total mass balance arises despite warmer T_{sfc} in INT (Fig. 7c). The inclusion of additional processes, such as the refreezing of meltwater, and the different

TCD
7, 103–144, 2013

method of subsurface temperature calculation both contribute to warmer T_{sfc} in both INT and OFF compared with the Noah LSM, with the difference expressed, again, primarily at night (+9.2 °C between 6:00 p.m.–8:00 a.m. LT). The changes in surface energy and mass fluxes underlying the difference in ablation are discussed below.

The vertical balance profile (VBP) on 31 August 2004, is shown in Fig. 8a, with areas of negative (positive) balance modelled below (above) ~ 5875 m. The altitudinal distribution is characterized by a shallowing of the VBP above ~ 5000 m, associated with (1) an increase in the positive vertical gradient of the fraction of solid precipitation that contributes positively to mass balance (Fig. 8c), and (2) cooling of mean surface temperature with height to below the melting point (cf. Fig. 2a). Above 5875 m, the VBP profile again steepens as a result of large increases in accumulated, solid precipitation. The vertical pattern of the influence of interactive coupling on modelled mass balance is generally a positive change: INT produces less ablation below 5875 m (on average, 117.7 mm w.e.), while above this level it simulates some mean increases in accumulation (13.4 mm w.e.) in part due to small increases in both accumulated precipitation and its frozen fraction (cf. Fig. 8b, c). Averaged over the whole period, the equilibrium line altitudes are 5469 and 5536 m in INT and OFF, respectively, which exceed the annual and generalized estimate of 4500 m by Hewitt (2005) and of 4200–4800 m by Young and Hewitt (1993), because we simulate the ablation season, only.

Figure 9 presents the surface fluxes of energy and mass from the interactive simulation. On average, the main energy sources are incoming radiation, $S\downarrow$ (374.3 W m^{-2}) and $L\downarrow$ (220.4), with smaller contributions from QS (9.5), QC (8.1) and a negligible QPRC (Fig. 9a). The main energy sinks are outgoing $L\uparrow$ (−306.1) and reflected $S\uparrow$ (−186.4), followed by QM (−74.0), QPS (−32.1), and QL (−13.9). Mass gains are, in general, dominated by refreeze (1.0 kg m^{-2}) and solid precipitation (0.9), with a negligible contribution from deposition (Fig. 9b). Mass loss is primarily through surface (−19.1) and subsurface (−3.2) melt, with a smaller contribution from sublimation (−0.5). Figure 9 also illustrates the main advantage of the coupled model: it elucidates the important physical processes behind a mass change signal that results from atmospheric

TCD
7, 103–144, 2013

forcing. As a simple example, the snowfall event that occurs at the beginning of August (cf. solid precipitation bars in Fig. 9b) is clearly associated with (1) a reduction in $S\downarrow$ and an increase in $L\downarrow$, (2) a spike in both surface albedo and thus $S\uparrow$, and (3) a reduction in absorbed shortwave radiation that translates into reduced energy for surface and subsurface melt. Furthermore, changes in glacier surface conditions have a noticeable feedback on the atmosphere during and after the snowfall event (cf. e.g. shortwave radiation curves in Fig. 5e or cloud fraction changes in Fig. 6d).

Interactive coupling has the strongest influence on the net shortwave and ground heat fluxes in the atmospheric model (Fig. 10a). The average QG in INT ($-23.7\,W\,m^{-2}$) greatly exceeds that simulated by the Noah LSM alone (−0.5), due to (1) the inclusion of penetrating shortwave radiation, which always represents an energy sink at the surface, and (2) warmer surface temperatures, which result in a stronger (more negative) flux downward to the subsurface. The difference contributes to soil temperatures in the top two meters that are on average 2.6 K warmer (cf. Fig. 6c). Mean absorbed shortwave radiation is also much larger in INT (184.8 vs. $107.9\,W\,m^{-2}$), as a result of lower average surface albedo (0.49 vs. 0.71; also see Fig. 2c) over the simulation period. Coupling also introduces small increases in both the net longwave radiation ($-0.9\,W\,m^{-2}$/1.0 %) and QL (2.0/16.7), while QS is reduced (2.1/−18.3). Changes in the turbulent heat fluxes also reflect different treatments of surface roughness, which is a spatially- and temporally-varying parameter in WRF-MB that ranges between 0.0008 and 0.0026 m as a function of snow age and generally exceeds the constant value of 0.001 m specified by the Noah LSM for snow/ice surfaces. The different formulations translate into a mean increase in effective roughness length (e.g. Eq. 7 in Braithwaite, 1995) of 0.00017 from 0.0021 in INT.

In the MB model, interactive coupling induces the largest magnitude change in the net short- and long-wave radiative fluxes, with SWnet decreasing by 3.3 % and LWnet increasing by 1.8 %, mainly as a result of the changes to $S\downarrow$ and $L\downarrow$ in the atmospheric model discussed previously. The MB model fluxes of QL and QPS decrease (become less negative) on average in INT by 8.9 % and 3.5 %, respectively (Fig. 10b). In addition,

TCD
7, 103–144, 2013

QC and QS are reduced, by 9.0 % and 5.0 %, respectively. The reduction in QPS is associated with less snow-cover-free glacier area in INT, which reduces the subsurface absorption of shortwave radiation (Mölg et al., 2008). The reduction in the turbulent heat fluxes appears to stem from reduced 10-m wind speeds (-0.2 to $4.3\,m\,s^{-1}$), due to the surface roughness changes discussed above. The changes also occur despite (1) a weaker correction for atmospheric stability on average, according to a modified version of the Monin–Obukhov stability function (Eq. 12 in Braithwaite, 1995) that increases by 0.1 to 0.83 in INT; and (2) stronger mean gradients in vapor pressure (ΔVP; -1.2 in INT vs. -0.7 hPa in OFF) and temperature (ΔT; 1.8 vs. 1.2 K) between the near surface and lower boundary. Note that variability in these gradients is suppressed in the interactive simulation when feedbacks are included: the standard deviation of ΔVP (ΔT) decreases from 1.2 (3.1) to 1.0 hPa (2.6 K) in INT.

The net result is a decrease of 4.8 % in the average energy available for surface melt, QM, and less negative mass balance over the INT simulation (cf. Fig. 7b). Therefore, the greatest absolute change in the mass fluxes in INT is a reduction in surface melt (-5.8 %; Fig. 10c). To a much smaller extent, sublimation (-9.0 %) and subsurface melt (-0.8 %) are also reduced. Furthermore, smaller melt production in INT is compounded by increases in both refreezing in the snowpack and the formation of superimposed ice (8.5 % combined), as well as by greater solid precipitation (4.0 %). In general, mass exchanges between the glacier surface and the overlying boundary layer are smaller in INT, with the reduction in QL resulting in less sublimation (particularly at night) and deposition (at all times).

3.4 Remarks and perspectives for future research

The explicit approach to modelling alpine glacier mass balance using WRF first demonstrated by Mölg and Kaser (2011) has been applied in offline mode for simulations of small glaciers (Mölg and Kaser, 2011; Mölg et al., 2012a,b) and has yielded important insights into the physical processes and the atmospheric forcing underlying mass fluctuations. However, here we demonstrate that feedbacks due to MB processes

TCD
7, 103–144, 2013

are evident for the heavily-glaciated Karakoram region. The basin-scale influence of interactive coupling on the atmospheric forcing data, while moderate, acts to reduce the energy available for surface melt and, in concert with both reduced mass exchanges between the surface and boundary layer and increased refreezing, reduces ablation during the summer of 2004. Thus, one potential implication of this study is that the traditional, or offline, approach tends to produce more negative total mass balance during the ablation season. However, our intent here is to demonstrate that the inclusion of additional real processes as well as MB feedbacks renders WRF-MB capable of simulating observed magnitudes of MB.

To the best of our knowledge, only one previous study, that of Kotlarski et al. (2010b), has performed interactive and distributed simulations of alpine glacier mass balance, achieved by introducing a subgrid-scale parameterization for glaciers and their areal changes into a regional climate model configured with a relatively coarse spatial resolution of ~ 18 km. However, their implicit treatment "pools" the glaciers located in a grid cell into one ice mass at a fixed altitude and with a uniform snow depth. Furthermore, they quantify the effect of two-way coupling by comparing their interactive simulation with a control run that contains no glaciers (i.e. snow and ice surfaces are compared with bare soil or vegetation-covered surfaces), thus obscuring the exact role of feedbacks. Therefore, this paper presents the first assessment of the importance and strength of interactions between alpine glaciers and the atmosphere on explicit simulations of mass balance.

We have shown results for only a short study period, of one ablation season, to evaluate the novel approach and its performance against the available measurements. The Karakoram, and the Himalayan region in general, are very data-sparse (e.g. Bolch et al., 2012), due to the expense and logistics of field surveys in this remote region. The model captures the magnitude of the 53 stake measurements of Mihalcea et al. (2006), and simulating the ablation season likely represents the greatest test for some of the simplifying assumptions employed, such as zero debris cover. However, a longer application is needed to assess the year-long and inter-annual influence of

TCD
7, 103–144, 2013

interactive coupling, as well as the long-term performance of the atmospheric model under the climate-simulation forcing strategy we employ (i.e. with no nudging or model re-initialization; e.g. Maussion et al., 2011). Simulations of snow mass balance are also inherently sensitive to the modelled solid precipitation (Mölg and Kaser, 2011), which is influenced in our study by the choice of microphysics scheme. The simulation of near-surface meteorological fields by WRF over glacier surfaces has been found to be relatively insensitive to the choice of physical parameterizations (Claremar et al., 2012); however, the extent to which modelled mass balance is dependent on both the model physics and the spatial resolution of the finest domain represents important uncertainties that will be explored in a future study.

The mean proportion of debris covered-area on Karakoram glaciers is estimated to be 18–22 % (Scherler et al., 2011; Hewitt, 2011), which is higher than the pan-Himalayan average of ∼ 10 % (Bolch et al., 2012). Specific to the Baltoro glacier, Mayer et al. (2006) estimate that ∼ 38 % of the total glacier area is debris covered. The presence of debris above a threshold, or "critical thickness", of ∼ 2 cm has been shown, empirically and through surface energy balance modelling, to reduce glacier ablation as a result of its insulating effect (e.g. Østrem, 1959; Kayastha et al., 2000; Nicholson and Benn, 2006; Reid et al., 2012). The range of mean debris thicknesses at the stake sites is 2.0–18.0 cm (Table 4), suggesting that on the whole insulation effects should dominate over the lowering of surface albedo. Therefore, the overestimation of ablation by WRF-MB is physically consistent with the exclusion of debris in this study. This interpretation is supported by the first distributed ablation modelling study for debris-covered ice, that of Reid et al. (2012), which found reduced sub-debris ablation when depth exceeded 2 cm. However, it is noteworthy that geodetic estimates of early 21st century thickness changes in the Karakoram (Gardelle et al., 2012; Kääb et al., 2012) do not show differential ablation between clean and debris-covered ice.

In order to allow the WRF-MB modelling system to provide long-term, accurate simulations in the Karakoram, the effects of debris cover on surface conditions and glacier ablation will need to be included. Treating debris cover in distributed mass balance

TCD
7, 103–144, 2013

modelling is also becoming more important in light of observations of increasing debris-covered area in many regions (e.g. Stokes et al., 2007; Bhambri et al., 2011). Another process that is thought to be important for Karakoram glaciers is accumulation via snow and ice avalanching (e.g. Hewitt, 2011), which may be useful to parameterize. Finally, dynamical ice flow changes have been shown to be important when quantifying the response of Himalayan glaciers to climate fluctuations on multiannual timescales (e.g. Scherler et al., 2011; Gardelle et al., 2012; Kääb et al., 2012; Azam et al., 2012).

4 Conclusion

MB feedbacks have been introduced into a new, multi-scale modelling approach for explicitly resolving the mass balance processes of alpine glaciers, and this technique has been extended to the regional scale. Although validation data is sparse, the model captures the magnitude of available in situ measurements, with improvements arising from including feedbacks from the MB model to WRF. Furthermore, discrepancies between observed and simulated ablation can be attributed to physical processes neglected as simplifying assumptions, particularly debris cover effects.

Both components of WRF-MB are based on physical principles, with no statistical downscaling at their interface. The direct linkage increases the applicability of this approach for the simulation of the paleo- and future-climate response of glaciers, since the modelling system produces a physically-consistent response to changes in external forcing. Incorporation of the MB model also increases the number of physical processes important for glaciers represented in the atmospheric model, and provides a consistent calculation of surface energy and mass fluxes, since changes in glacier surface conditions are permitted to influence the atmospheric drivers. Perhaps the most important advantage, however, is that WRF-MB permits direct causal attribution of glacier mass changes to both physical processes and the main atmospheric drivers. With further development, the model has the potential to bridge the data gap in the

TCD
7, 103–144, 2013

Karakoram and shed light on the role of climate forcing in the anomalous behaviour of glaciers in this region.

The offline approach to simulations of MB, as well as the simplified representation of glaciers in regional atmospheric models, essentially treats either the atmosphere or alpine glaciers simply as a boundary condition. We suggest that this unified, explicit approach should be increasingly adopted in future studies, particularly for heavily glaciated regions.

Acknowledgements. E. Collier was supported by a Natural Sciences and Engineering Research Council of Canada (NSERC) CGS-D award, a NSERC Michael Smith Foreign Study Scholarship, and an Alberta Ingenuity Graduate Student Scholarship. T. Mölg was supported by the Alexander von Humboldt Foundation. F. Maussion and D. Scherer acknowledge support from the German Research Foundation (DFG) Priority Programme 1372 under the code SCHE 750/4-3, and the German Federal Ministry of Education and Research (BMBF) Programme CAME under the code 03G0804A. A.B.G. Bush acknowledges support from NSERC and from the Canadian Institute for Advanced Research. The supercomputing resources for this study were provided by Compute/Calcul Canada. We would like to thank Ev-K2-CNR for providing the meteorological data from the Baltoro glacier, together with the University of Milan for supporting the field work.

References

Azam, M. F., Wagnon, P., Ramanathan, A., Vincent, C., Sharma, P., Arnaud, Y., Linda, A., Pottakkal, J. G., Chevallier, P., Singh, V. B., and Berthier, E.: From balance to imbalance: a shift in the dynamic behaviour of Chhota Shigri glacier, western Himalaya, India, J. Glaciol., 58, 315–324, 2012. 124

Bhambri, R., Bolch, T., Chaujar, R. K., and Kulshreshtha, S. C.: Glacier changes in the Garhwal Himalaya, India, from 1968 to 2006 based on remote sensing, J. Glaciol., 57, 543–556, 2011. 124

Bolch, T., Kulkarni, A., Kääb, A., Huggel, C., Paul, F., Cogley, J. G., Frey, H., Kargel, J. S., Fujita, K., Scheel, M., Bajracharya, S., and Stoffel, M.: The state and fate of Himalayan glaciers, Science, 336, 310–314, 2012. 106, 108, 122, 123

TCD

7, 103–144, 2013

Braithwaite, R. J.: Aerodynamic stability and turbulent sensible-heat flux over a melting ice surface, the Greenland ice sheet, J. Glaciol., 41, 562–571, 1995. 120, 121
Brodzik, M. J., Armstrong, R., and Savoie, M.: Global EASE-Grid 8-day Blended SSM/I and MODIS Snow Cover, National Snow and Ice Data Center, Boulder, Colorado, USA, Digital media, 2007. 109
Chen, F. and Dudhia, J.: Coupling an advanced land surface-hydrology model with the Penn State – NCAR MM5 modelling system. Part I: Model implementation and sensitivity, Mon. Weather Rev., 129, 569–585, 2001. 108, 110
Claremar, B., Obleitner, F., Reijmer, C., Pohjola, V., Waxegård, A., Karner, F., and Rutgersson, A.: Applying a mesoscale atmospheric model to Svalbard glaciers, Adv. Meteorol., 2012, 321649, doi:10.1155/2012/321649, 2012. 123
Cogley, J. G.: Present and future states of Himalaya and Karakoram glaciers, Ann. Glaciol., 52, 69–73, 2011. 106
Dee, D. P., Uppala, S. M., Simmons, A. J., Berrisford, P., Poli, P., Kobayashi, S., Andrae, U., Balmaseda, M. A., Balsamo, G., Bauer, P., Bechtold, P., Beljaars, A. C. M., van de Berg, L., Bidlot, J., Bormann, N., Delsol, C., Dragani, R., Fuentes, M., Geer, A. J., Haimberger, L., Healy, S. B., Hersbach, H., Hlm, E. V., Isaksen, L., Kållberg, P., Köhler, M., Matricardi, M., McNally, A. P., Monge-Sanz, B. M., Morcrette, J.-J., Park, B.-K., Peubey, C., de Rosnay, P., Tavolato, C., Thpaut, J.-N., and Vitart, F.: The ERA-Interim reanalysis: configuration and performance of the data assimilation system, Q. J. Roy. Meteor. Soc., 137, 553–597, 2011. 108
Frey, H., Paul, F., and Strozzi, T.: Compilation of a glacier inventory for the western Himalayas from satellite data: methods, challenges, and results, Remote Sens. Environ., 124, 832–843, 2012. 108
Gardelle, J., Berthier, E., and Arnaud, Y.: Slight mass gain of Karakoram glaciers in the early twenty-first century, Nat. Geosci., 5, 322–325, 2012. 106, 107, 123, 124
Gardner, A. S., Sharp, M. J., Koerner, R. M., Labine, C., Boon, S., Marshal, S. J., Burgess, D. O., and Lewis, E.: Near-surface temperature lapse rates over Arctic glaciers and their implications for temperature downscaling, J. Climate, 22, 4281–4298, 2009. 105
Hewitt, K.: The Karakoram anomaly? Glacier expansion and the "elevation effect" Karakoram Himalaya, Mt. Res. Dev., 25, 332–340, 2005. 106, 119
Hewitt, K.: Glacier change, concentration, and elevation effects in the Karakoram Himalaya, Upper Indus Basin, Mt. Res. Dev., 31, 188–200, 2011. 123, 124

TCD
7, 103–144, 2013

ICIMOD (International Centre for Integrated Mountain Development): Inventory of glaciers, glacial lakes and identification of potential glacial lake outburst floods (GLOFs), affected by global warming in the Mountains of Himalayan Region, Kathmandu, DVD-ROM, 2007. 108

Jiménez, P. A., Dudhia, J., González-Rouco, J. F., Navarro, J., Montávez, J. P., and García-Bustamante, E.: A revised scheme for the WRF surface layer formulation, Mon. Weather Rev., 140, 898–918, 2012. 109

Kääb, A., Berthier, E., Nuth, C., Gardelle, J., and Arnaud, Y.: Contrasting patterns of early twenty-first-century glacier mass change in the Himalayas, Nature, 488, 495–498, 2012. 106, 107, 123, 124

Kayastha, R. B., Takeuchi, Y., Nakawo, M., and Ageta, Y.: Practical prediction of ice melting beneath various thickness of debris cover on Khumbu Glacier, Nepal using a positive degree-day factor, Symposium at Seattle 2000 – Debris-Covered Glaciers, IAHS Publ., 264, 71–81, 2000. 123

Kotlarski, S., Paul, F., and Jacob, D.: Forcing a distributed glacier mass balance model with the regional climate model REMO. Part I: Climate model evaluation, J. Climate, 23, 1589–1606, 2010a. 105

Kotlarski, S., Jacob, D., Podzum, R., and Paul, F.: Representing glaciers in a regional climate model, Clim. Dynam., 34, 27–46, 2010b. 105, 106, 122

Knievel, J. C., Bryan, G. H., and Hacker, J. P.: Explicit numerical diffusion in the WRF model, Mon. Weather Rev., 135, 3808–3824, 2007. 109

Paul, F. and Kotlarski, S.: Forcing a distributed glacier mass balance model with the regional climate model REMO. Part II: Downscaling strategy and results for two Swiss glaciers, J. Climate, 23, 1607–1620, 2010. 105

Livneh, B., Xia, Y., Mitchell, K. E., Ek, M. B., and Lettenmaier, D. P.: Noah LSM snow model diagnostics and enhancements, J. Hydrometeorol., 11, 721–738, 2009. 114

Machguth, H., Paul, F., Kotlarski, S., and Hoelzle, M.: Calculating distributed glacier mass balance for the Swiss Alps from regional climate model output: a methodical description and interpretation of the results, J. Geophys. Res., 114, D19106, doi:10.1029/2009JD011775, 2009. 104, 105

Marshall, S. J., Sharp, M. J., Burgess, D. O., and Anslow, F. S.: Surface temperature lapse rate variability on the Prince of Wales Ice-eld, Ellesmere Island, Canada: implications for regional-scale downscaling of temperature, Int. J. Climatol., 27, 385–398, 2007. 105

TCD
7, 103–144, 2013

Maussion, F., Scherer, D., Finkelnburg, R., Richters, J., Yang, W., and Yao, T.: WRF simulation of a precipitation event over the Tibetan Plateau, China – an assessment using remote sensing and ground observations, Hydrol. Earth Syst. Sci., 15, 1795–1817, doi:10.5194/hess-15-1795-2011, 2011. 105, 123

Mayer, C., Lambrecht, A., Belo, M., Smiraglia, C., and Diolaiuti, G.: Glaciological characteristics of the ablation zone of Baltoro glacier, Karakoram, Pakistan, Ann. Glaciol., 43, 123–131, 2006. 112, 114, 116, 117, 123

Mihalcea, C., Mayer, C., Diolaiuti, G., Smiraglia, C., and Tartari, G.: Ablation conditions on the debris covered part of Baltoro Glacier, Karakoram, Ann. Glaciol., 43, 292–300, 2006. 112, 113, 122

Mihalcea, C., Mayer, C., Diolaiuti, G., DAgata, C., Smiraglia, C., Lambrecht, A., Vuillermoz, E., and Tartari, G.: Spatial distribution of debris thickness and melting from remote-sensing and meteorological data, at debris-covered Baltoro glacier, Karakoram, Pakistan, Ann. Glaciol., 48, 49–57, 2008. 116, 117

Molinari, J. and Dudek, M.: Parameterization of convective precipitation in mesoscale numerical-models – a critical-review, Mon. Weather Rev., 120, 326–344, 1992. 108

Mölg, T. and Kaser, G.: A new approach to resolving climate–cryosphere relations: downscaling climate dynamics to glacier-scale mass and energy balance without statistical scale linking, J. Geophys. Res., 116, D16101, doi:10.1029/2011JD015669, 2011. 104, 105, 106, 108, 109, 121, 123

Mölg, T., Cullen, N. J., Hardy, D. R., Kaser, G., and Klok, E. J.: Mass balance of a slope glacier on Kilimanjaro and its sensitivity to climate, Int. J. Climatol., 28, 881–892, 2008. 107, 109, 121

Mölg, T., Cullen, N. J., Hardy, D. R., Winkler, M., and Kaser, G.: Quantifying climate change in the tropical midtroposphere over East Africa from glacier shrinkage on Kilimanjaro, J. Climate, 22, 4162–4181, 2009. 107, 109

Mölg, T., Maussion, F., Yang, W., and Scherer, D.: The footprint of Asian monsoon dynamics in the mass and energy balance of a Tibetan glacier, The Cryosphere, 6, 1445–1461, doi:10.5194/tc-6-1445-2012, 2012a. 105, 107, 109, 111, 121, 132

Mölg, T., Grohauser, M., Hemp, A., Hofer, M., and Marzeion, B.: Limited forcing of glacier loss through land-cover change on Kilimanjaro, Nat. Clim. Change, 2, 254–258, 2012b. 105, 117, 121

TCD
7, 103–144, 2013

Nicholson, L. and Benn, D.: Calculateing ice melt beneath a debris layer using meteorological data, J. Glaciol., 52, 463–470, 2006. 123
Niu, G.-Y., Yang, Z.-L., Mitchell, K. E., Chen, F., Ek, M. B., Barlage, M., Kumar, A., Manning, K., Niyogi, D., Rosero, E., Tewari, M., and Youlong, X.: The community Noah land surface model with multiparameterization options (Noah-MP): 1. Model description and evaluation with local-scale measurements, J. Geophys. Res., 116, D12109, doi:10.1029/2010JD015139, 2011. 111
Oerlemans, J. and Knap, W. H.: A 1 year record of global radiation and albedo in the ablation zone of Morteratschgletscher, Switzerland, J. Glaciol., 44, 231–238, 1998. 114
Østrem, G.: Ice melting under a thin layer of moraine, and the existence of ice cores in moraine ridges, Geogr. Ann., 41, 228–230, 1959. 123
Petersen, L. and Pellicciotti, F.: Spatial and temporal variability of air temperature on a melting glacier: atmospheric controls, extrapolation methods and their effect on melt modeling, Juncal Norte Glacier, Chile, J. Geophys. Res., 116, D23109, doi:10.1029/2011JD015842, 2011. 105
Pritchard, M. S., Bush, A. B. G., and Marshall, S. J.: Neglecting ice-atmosphere interactions underestimates ice sheet melt in millennial-scale deglaciation simulations, Geophys. Res. Lett., 35, L01503, doi:10.1029/2007GL031738, 2008. 106
Radić, V., and Hock, R.: Regionally differentiated contribution of mountain glaciers and ice caps to future sea-level rise, Nat. Geosci., 4, 91–94, 2011. 105
Reid, T. D., Carenzo, M., Pellicciotti, F., and Brock, B. W.: Including debris cover effects in a distributed model of glacier ablation, J. Geophys. Res., 117, D18105, doi:10.1029/2012JD017795, 2012. 105, 123
Ridley, J. K., Huybrechts, P., Gregory, J. M., and Lowe, J. A.: Elimination of the Greenland ice sheet in a high CO_2 climate, J. Climate, 18, 3409–3427, 2005. 106
Scherler, D., Bookhagen, B., and Strecker, M. R.: Spatially variable response of Himalayan glaciers to climate change affected by debris cover, Nat. Geosci., 4, 156–159, 2011. 106, 114, 123, 124
Shi, Y., Liu, C., and Kang, E.: The glacier inventory of China, Ann. Glaciol., 50, 1–4, 2009. 108
Skamarock, W. C. and Klemp, J. B.: A time-split nonhydrostatic atmospheric model for weather research and forecasting applications, J. Comput. Phys., 227, 3465–3485, 2008. 107, 109

TCD
7, 103–144, 2013

Stokes, C. R., Popovnin, V., Aleynikov, A., Gurney, S. D., and Shahgedanova, M.: Recent glacier retreat in the Caucasus Mountains, Russia, and associated increase in supraglacial debris cover and supra-/proglacial lake development, Ann. Glaciol., 46, 195–203, 2007. 124

Stroeve, J. C., Box, J. E., and Haran, T.: Evaluation of the MODIS (MOD10A1) daily snow albedo product over the Greenland ice sheet, Remote Sens. Environ., 105, 155–171, 2006. 115

van Pelt, W. J. J., Oerlemans, J., Reijmer, C. H., Pohjola, V. A., Pettersson, R., and van Angelen, J. H.: Simulating melt, runoff and refreezing on Nordenskiöldbreen, Svalbard, using a coupled snow and energy balance model, The Cryosphere, 6, 641–659, doi:10.5194/tc-6-641-2012, 2012. 105

Weisman, M. L., Skamarock, W. C., and Klemp, J. B.: The resolution dependence of explicitly modeled convective systems, Mon. Weather Rev., 125, 527–548, 1997. 108

Yao, T.: Map of the Glaciers and Lakes on the Tibetan Plateau and Adjoining Regions, Xian Cartographic Publishing House, Xian, China, 2007. 106

Young, G. J. and Hewitt, K.: Glaciohydrological features of the Karakoram Himalaya: measurement possibilities and constraints, in: Proceedings of the Kathmandu Symposium – Snow and Glacier Hydrology, IAHS Publ., 218, 273–283, 1993. 119

Table 1. WRF configuration.

Model domains	
Horizontal grid spacing	33, 11, 2.2 km (domains 1–3)
Time step	60, 20, 4 s
Vertical levels	40
Height of lowest model level	20 m
Model top pressure	25 hPa
Model physics	
Radiation	CAM
Microphysics	Thompson
Cumulus	Kain–Fritsch (none in D3)
Atmospheric boundary layer	Yonsei University
Surface layer	Monin–Obukhov (revised MM5)
Land surface	Noah version 3.1
Dynamics	
Top boundary condition	w-Rayleigh damping
Horizontal advection	Explicit 6th order coeff: 0.12, 0.12, 0.36
Lateral boundaries	
Specified boundary width	10 grid points
Relaxation exponent	0.33
Forcing	ERA Interim, 0.75 × 0.75° updated 6-hourly

TCD
7, 103–144, 2013

Table 2. MB model configuration.

Vertical levels (14)	0, 0.1, 0.2, 0.3, 0.4, 0.5, 0.8, 1, 1.4, 2, 3, 5, 7, 9 m
Fresh snow density	250 $kg\,m^{-2}$
Ice density	900 $kg\,m^{-2}$
Albedo scheme parameters	Mölg et al. (2012a)
Ice albedo	0.30
Firn albedo	0.55
Fresh snow albedo	0.85
Time scale	6.0 days
Depth scale	8.0 cm

TCD
7, 103–144, 2013

Table 3. Summary of available ablation stake measurements.

Stake section (Symbol) [Num. Stakes]	Measurement period (2004)	Mean location	Mean elevation (m a.s.l.)
Urdukas (U) [4]	2–15 July	76.285° E, 35.737° N	3993 [WRF: 4202]
Longitudinal Sect. 1 (L1) [2]	3–14 July	76.328° E, 35.740° N	4120 [WRF: 4201]
Stake Farm (SF) [23]	4–14 July	76.362° E, 35.737° N	4177 [WRF: 4262]
Gore 1 (G1) [4]	4–13 July	76.364° E, 35.739° N	4182 [WRF: 4303]
Longitudinal Sect. 2 (L2) [4]	5–12 July	76.418° E, 35.742° N	4308 [WRF: 4347]
Longitudinal Sect. 3 (L3) [2]	8–11 July	76.486° E, 35.739° N	4470 [WRF: 4601]
Concordia (C) [5]	8–11 July	76.502° E, 35.742° N	4537 [WRF: 4622]
Baltoro South (BS) [5]	7–11 July	76.538° E, 35.724° N	4634 [WRF: 4704]
Baltoro North (BN) [4]	8–11 July	76.520° E, 35.766° N	4646 [WRF: 4760]

TCD
7, 103–144, 2013

Table 4. Ablation rates (cm day^{-1}) and debris thickness.

Site	INT	OFF	Average measured (ice)	Mean debris thickness (cm)
U	−5.6	−5.5	−3.9	8.6
L1	−5.4	−5.3	−3.5	7.0
SF	−5.2	−5.1	−4.3	3.8
G1	−5.2	−5.1	−2.9	18.0
L2	−5.1	−5.1	−4.8	2.5
L3	−5.0	−4.9	−4.3	2.0
C	−4.9	−4.9	−2.9	6.0
BS	−6.4	−5.6	−1.8	6.8
BN	−7.4	−7.7	−1.8	7.8

TCD
7, 103–144, 2013

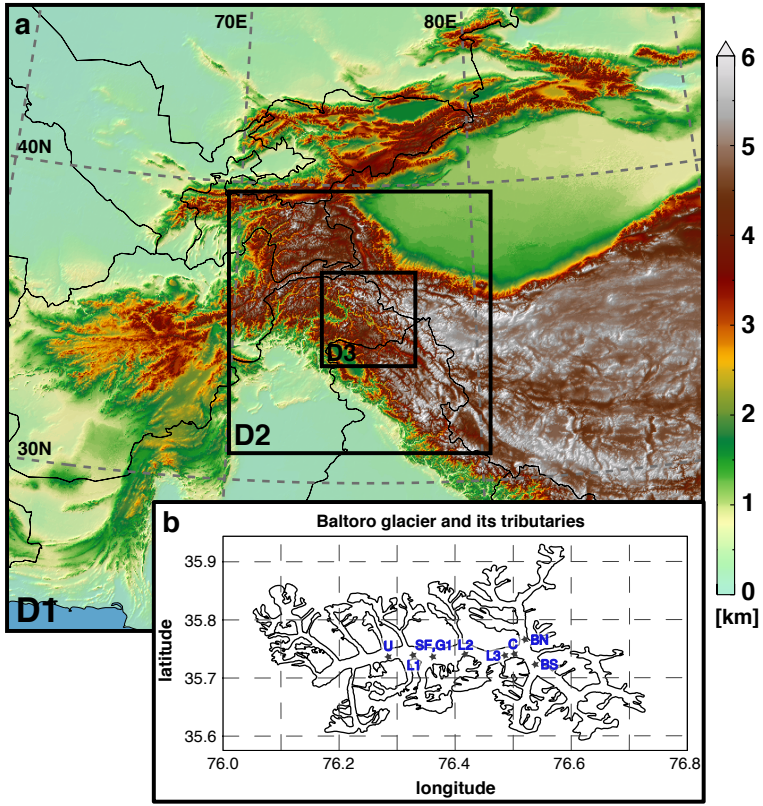

Fig. 1. (a) WRF atmospheric model domains, configured with horizontal spatial resolutions of 33-, 11-, and 2.2-km. Terrain elevation from the GTOPO30 dataset is shaded in units of meters. **(b)** Outline of Baltoro glacier and its tributaries, which are included in WRF D3, with the mean stake locations labeled and denoted by stars.

TCD
7, 103–144, 2013

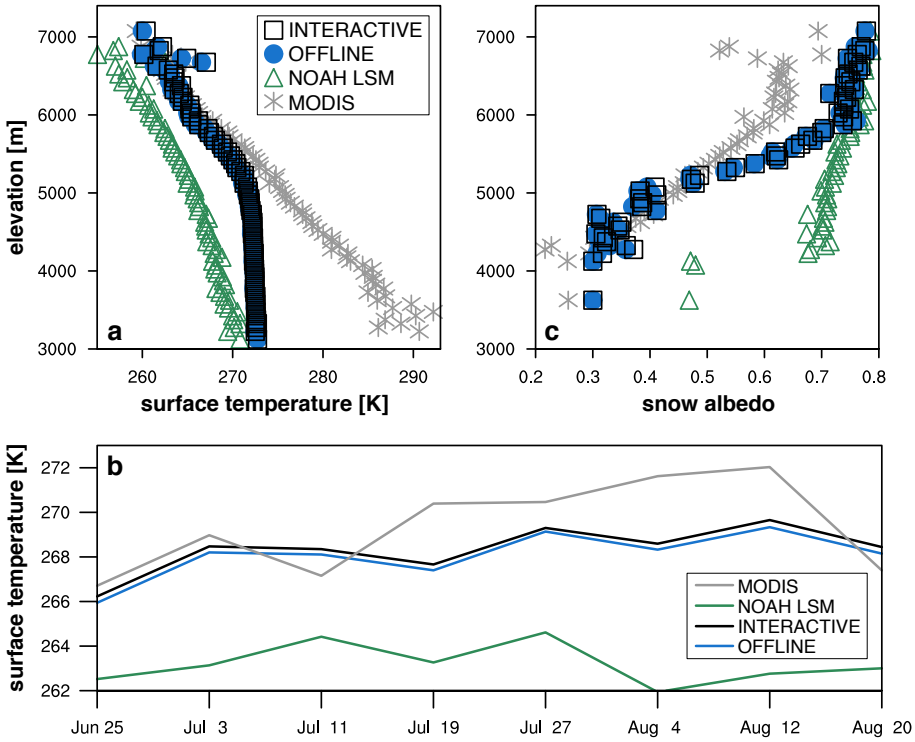

Fig. 2. Comparison between WRF-MB, Noah LSM, and MODIS for land surface temperature, **(a)** averaged from 25 June–28 August 2004, and in 50-m elevation bins, and **(c)** the mean time series above 5200 m elevation; and for **(b)** snow albedo, averaged between 25 June–31 August 2004, over glacier grid cells where at least 25 % of the daily times are available.

TCD
7, 103–144, 2013

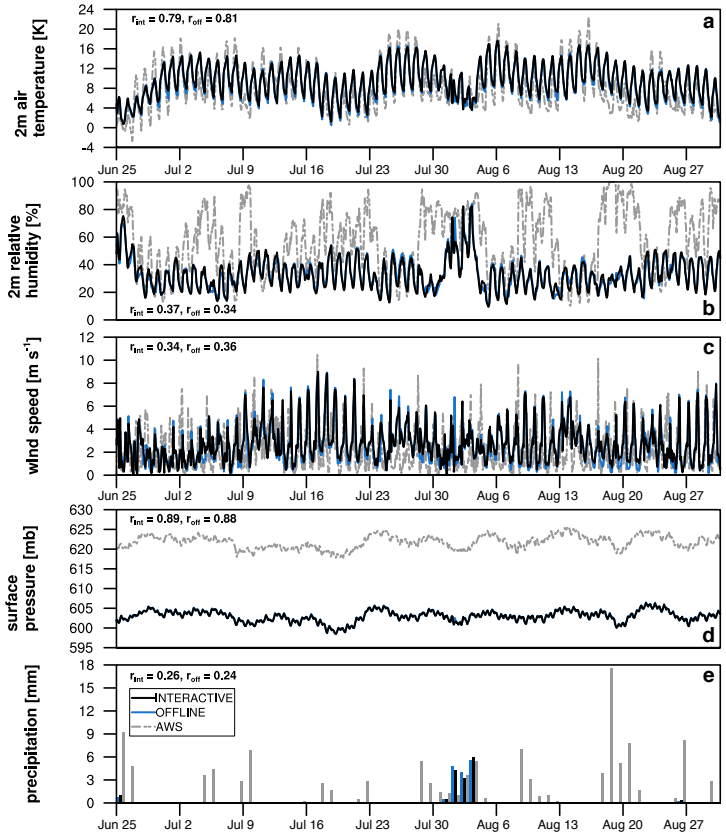

Fig. 3. Hourly **(a)** air temperature at 2 m, **(b)** relative humidity at 2 m, **(c)** wind speed at 10 m, **(d)** air pressure, and **(e)** daily total precipitation. Solid black (blue) curves display data from the interactive (offline) simulations while the dashed grey curve is the Urdukas AWS station data. Note that the offset in surface pressure arises from the difference in elevation of the AWS (4022 m a.s.l.) and the terrain height in the closest WRF grid cell (4322 m).

TCD
7, 103–144, 2013

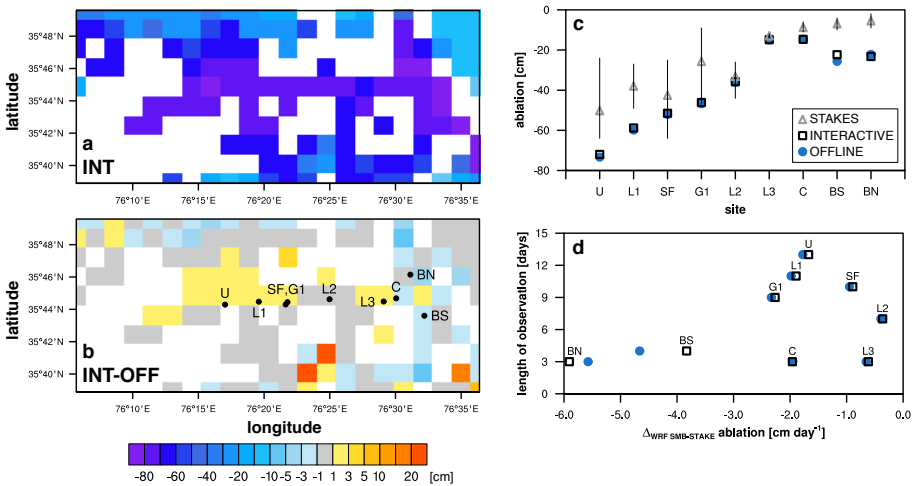

Fig. 4. (a) Total and **(b)** INT-OFF surface height change between 1–15 July 2004, in the vicinity of the main tongue of the Baltoro glacier. Stake site and transect locations shown in **(b)**, with additional information provided in Table 3. White grid cells correspond to non-glaciated area. **(c)** Measured mean ablation (triangles) at stake locations, with range of observed values denoted by bars. Simulated INT (OFF) ablation shown by black squares (blue circles). **(d)** Overestimation of ablation by WRF-MB versus the length of the observation period.

TCD
7, 103–144, 2013

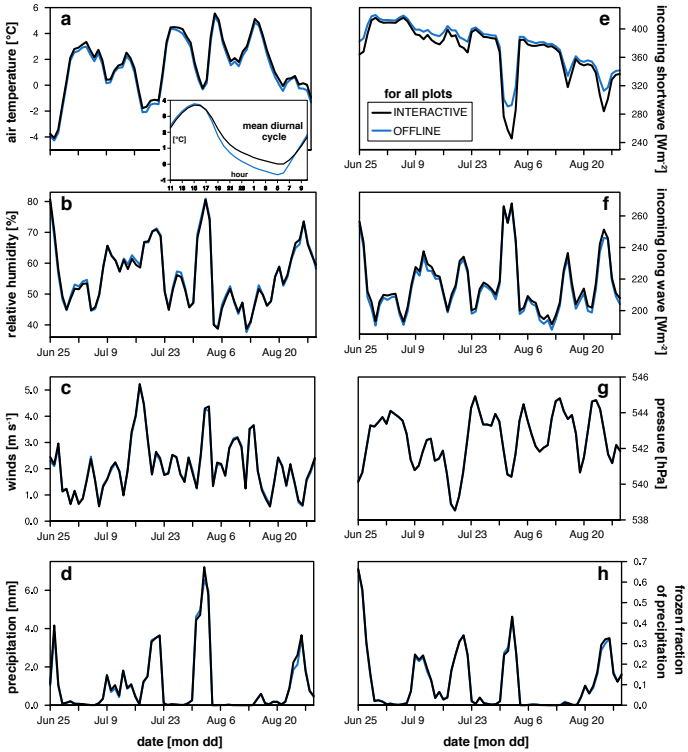

Fig. 5. Daily mean **(a)** air temperature, **(b)** relative humidity, **(c)** wind speed, **(d)** total precipitation, incoming **(e)** normal shortwave and **(f)** downward longwave radiation at ground surface, **(g)** air pressure, and **(h)** frozen fraction of precipitation, area-averaged over all glaciated grid cells. Data for **(a–c)**, and **(g)** are taken from the lowest model level ($z = 20$ m). The subpanel in **(a)** presents the average diurnal temperature cycle over the simulation period. Black (blue) curves display data from the interactive (offline) simulation.

TCD
7, 103–144, 2013

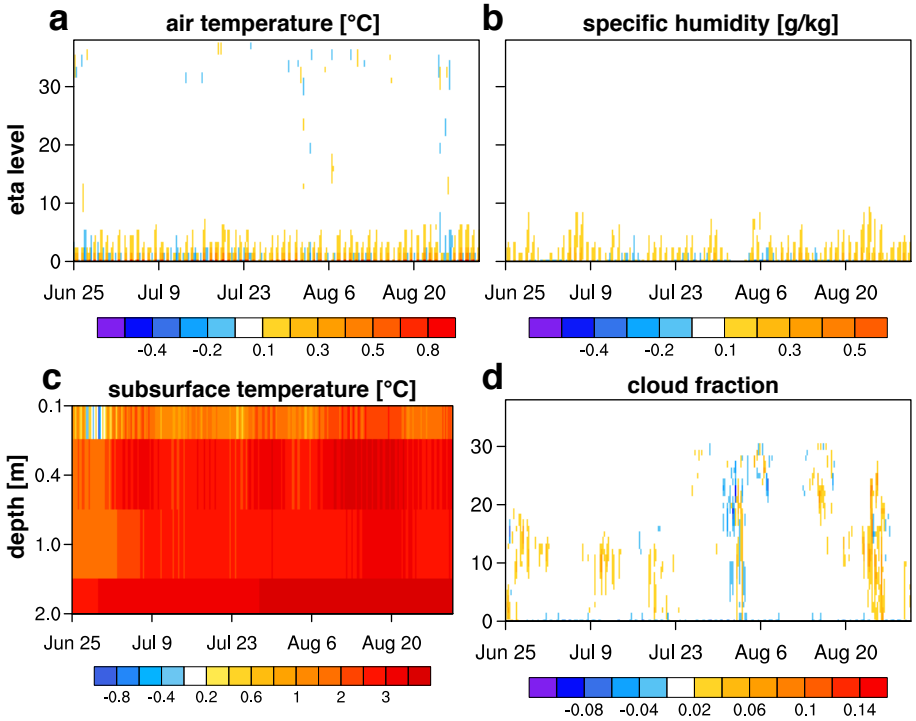

Fig. 6. Vertical and subsurface distribution of the influence of interactive coupling over glaciated areas illustrated by hourly time series of the change (INT-OFF) in area-averaged **(a)** air temperature,**(b)** specific humidity, **(c)** subsurface temperature, and **(d)** cloud fraction.

TCD
7, 103–144, 2013

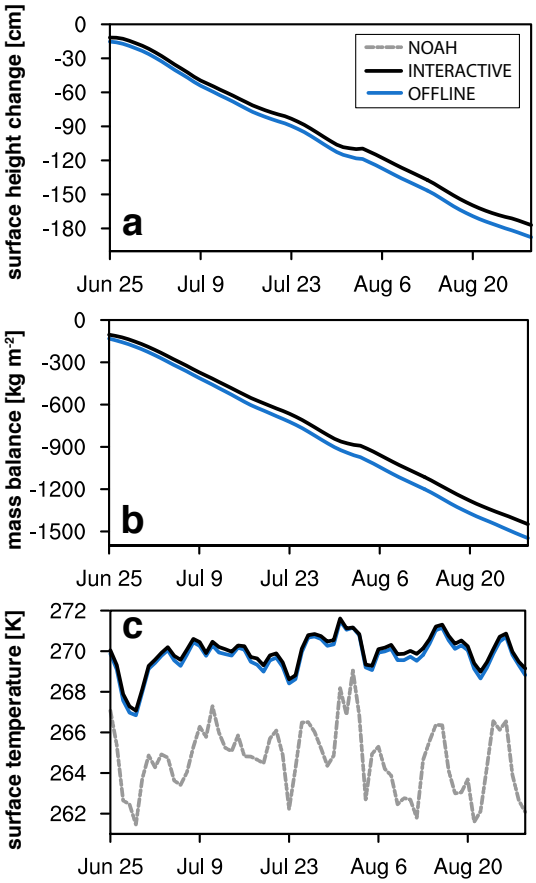

Fig. 7. Daily averages of **(a)** surface height change, **(b)** total mass balance, and **(c)** surface temperature. Black (blue) curves display data from the interactive (offline) simulation. For reference, surface temperature simulated by the Noah LSM is the dashed grey curve in **(c)**.

TCD
7, 103–144, 2013

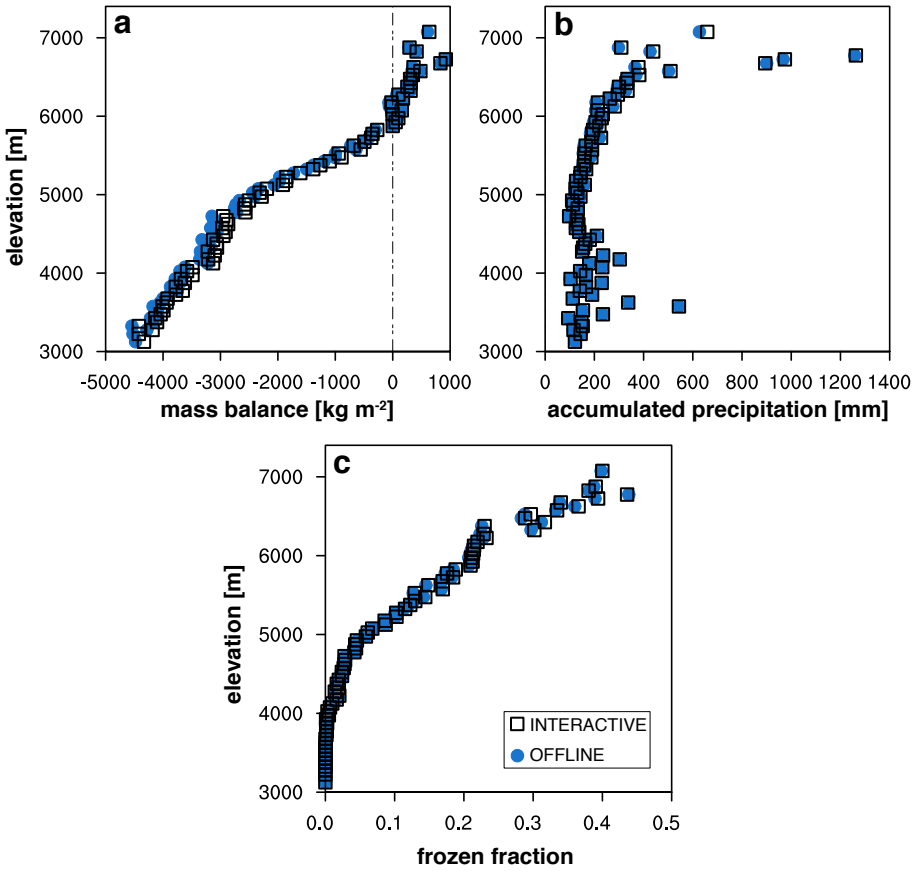

Fig. 8. (a) The vertical mass balance profile of the Karakoram basin at the end of the simulation. The altitudinal dependence of **(b)** total accumulated precipitation, and **(c)** mean frozen fraction, averaged over the simulation. Data are area-averaged in 50 m elevation bins.

TCD
7, 103–144, 2013

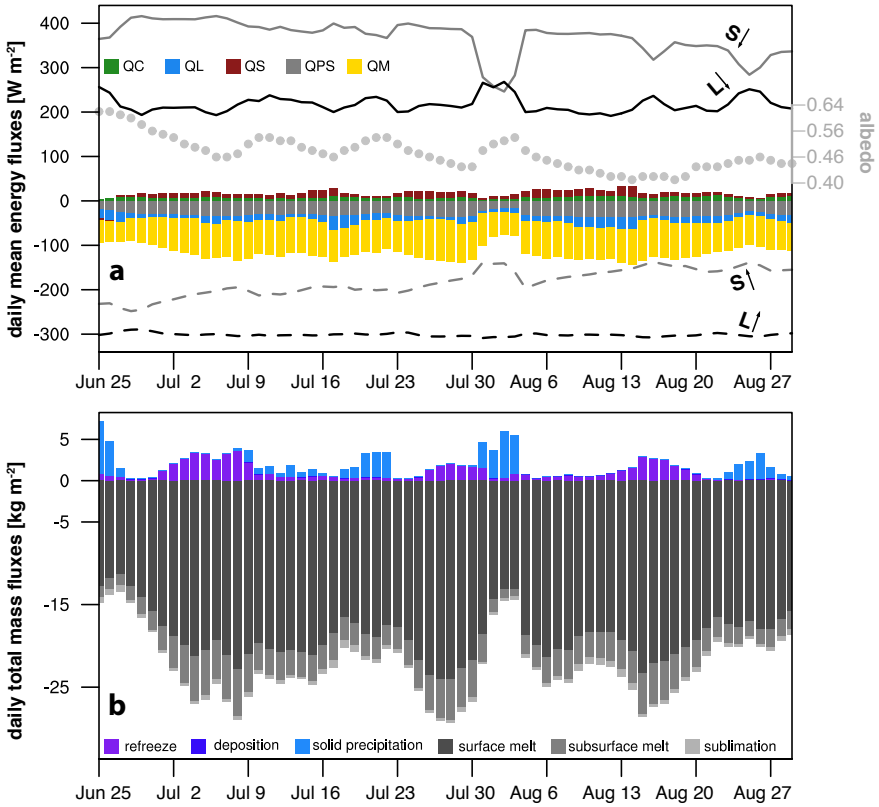

Fig. 9. From the interactive WRF-MB simulation: daily **(a)** mean surface energy balance components (left y-axis; see Eq. 1 for explanation of symbols) and albedo values (grey right y-axis), and **(b)** sums of mass fluxes. The radiation variables are shown in **(a)** as solid (directed downward) and dashed (upward) lines, albedo as grey dots, and the other surface energy fluxes as bars. The heat flux from precipitation (QPRC) is negligible and not shown. Values are averaged over glaciated grid cells only.

TCD
7, 103–144, 2013

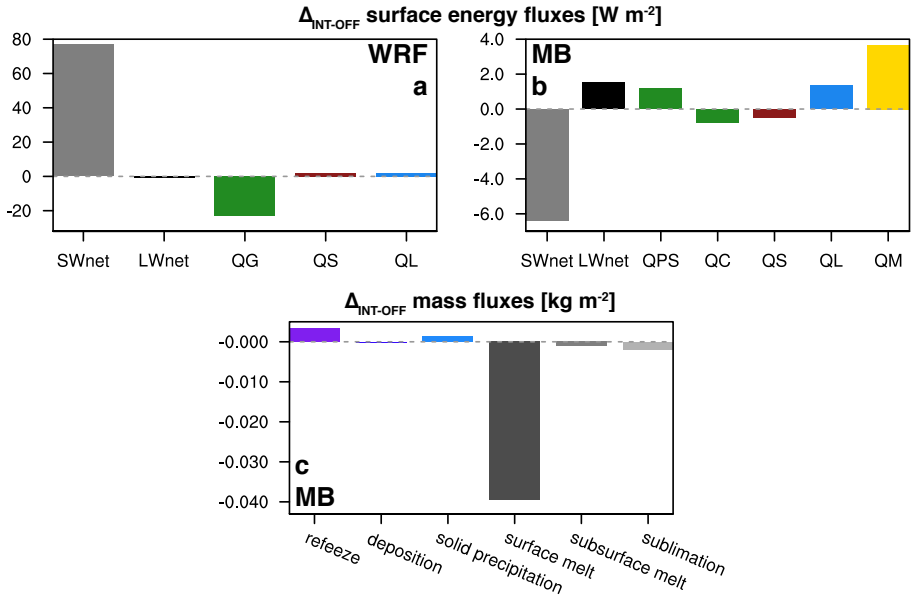

Fig. 10. Area-averaged mean difference (INT – OFF) over the simulation period and over glaciated grid cells of **(a)** the main components of the WRF surface energy budget, **(b)** the MB model energy fluxes, and **(c)** the MB model mass fluxes. Symbols in **(a)** represent, from left to right, net short- and long-wave radiation, ground heat flux, and turbulent fluxes of sensible and latent heat. Note that the sign convention for the turbulent fluxes in **(a)** is opposite to **(b)**. Symbols in **(b)** are discussed in Sect. 2.2

TCD
7, 103–144, 2013